Investigating the Intrinsic Attenuation of Large Low-Velocity Provinces

Donovan Marc Cunion

Advisor: Vedran Lekic

GEOL 394

Department of Geology

University of Maryland

04/29/2025

Contents

Abstract

At the base of the mantle, two massive, anomalously seismically slow regions (LLVPs) were discovered; however, their nature, origin, and role in global mantle dynamics are still debated. Seismic waves exhibit a notable velocity drop when traversing these structures, a characteristic commonly explained by thermochemical heterogeneities (Zhao et al., 2015). However, inferences of temperature and composition from velocity constraints are inherently nonunique. Observations of the attenuation experienced by seismic waves as they travel through LLVPs can be coupled with velocity measures providing additional information on their temperature, as attenuation is expected to increase exponentially with temperature (Jackson and Anderson, 1970). While elevated temperatures inside LLVPs inferred from their velocity reductions would imply higher attenuation, estimates of attenuation within LLVPs remain debated. The first 3D attenuation models of the lower mantle seemed to support this expectation (Lawrence and Wysession, 2006). However, recent studies based on normal modes argue that attenuation is lower in LLVPs than in the surrounding mantle (Talavera-Soza et al., 2025), suggesting that grain size, rather than temperature, plays a dominant role in controlling attenuation variations in the lower mantle. Here, published databases of body wave attenuation measurements (Lai and Garnero, 2019, 2020), specifically t* of S and ScS phases, sensitive to the lowermost mantle structure are analyzed in relation to LLVP location data. The effects of upper mantle attenuation variations are corrected using differential t* of reference phases and corrections based on published attenuation models. In the findings of this study, LLVP areas appear to be characterized by larger t* values, i.e., higher attenuation compared to regions outside the LLVPs. Results are discussed here in the context of previously published models of lower mantle attenuation and discuss potential implications for causative mechanisms.

Plain Language Abstract

At the core-mantle boundary, two continental-scale structures have disrupted the idea of a homogeneous mantle. These large structures were discovered from the slowing effect they have on seismic waves and named large low-velocity provinces (LLVPs). The shape and size of these regions have been determined by tracking the velocity changes in earthquake-generated waves as they travel through the Earth. Despite the increasing certainty of the overall shape of these provinces, the origin and cause of slowing seismic waves is still unknown. The common interpretation of why these structures slow seismic waves is that they are hotter and denser than the surrounding mantle. Hotter materials would also reduce the strength of seismic waves to a greater extent. This reduction in wave strength is measured as attenuation. Early models of the lower mantle support this interpretation; however, recent studies may show the opposite. Earlier this year, a paper from Utrecht University claimed that attenuation was lower in LLVPs than in the surrounding mantle because of large grain sizes (Talavera-Soza et al., 2025). The aim of this research is to compare published databases of body wave attenuation measurements to LLVP location data to find the relative attenuating effect these structures have. Results are interpreted as LLVPs with higher attenuation than the surrounding lower mantle.

Introduction

Large Low-Velocity Provinces

The Large Low-Velocity Provinces (LLVPs) under the Central Pacific and Africa (Fig. 1) are massive, seismically slow regions in the lower mantle. They are named Jason and Tuzo, respectively after W. Jason Morgan and J. Tuzo Wilson (Burke, 2011). These provinces range from 800 km deep to the core-mantle-boundary (CMB) and represent 3-8% of the volume of the Earth (Cottaar and Lekic, 2016). They were initially glimpsed as large-scale regions of lower-than-average shear wave velocity (V_S) in some of the earliest tomographic models of the lower mantle (e.g. Dziewoński, 1984), and their properties clarified with improvements in the resolution of tomographic models through the 1990s (e.g. Dziewoński et al., 1993, Su et al., 1994; Li and Romanowicz, 1996; Masters et al. 1996). Improved tomographic models of compressional wave velocity (V_P) variations, however, revealed that the slow wave speeds could be primarily attributed to shear modulus reductions, rather than the bulk modulus, which did not appear to be anomalously low in these regions (e.g. Su and Dziewoński, 1997; Masters et al. 2000). Because both V_P and V_S are affected by shear modulus, the term LLVP became increasingly prevalent over their previous name, Large Low Shear Velocity Provinces (LLSVPs). The primary research goals surrounding LLVPs have been the source of their heterogeneity, longevity, role in mantle dynamics, and lateral extent (e.g., Garnero et al., 2016). Over 40 years of research have culminated in a robust understanding of the locations and velocity structure of these provinces, however, their nature, role, and origin are still heavily debated among researchers.

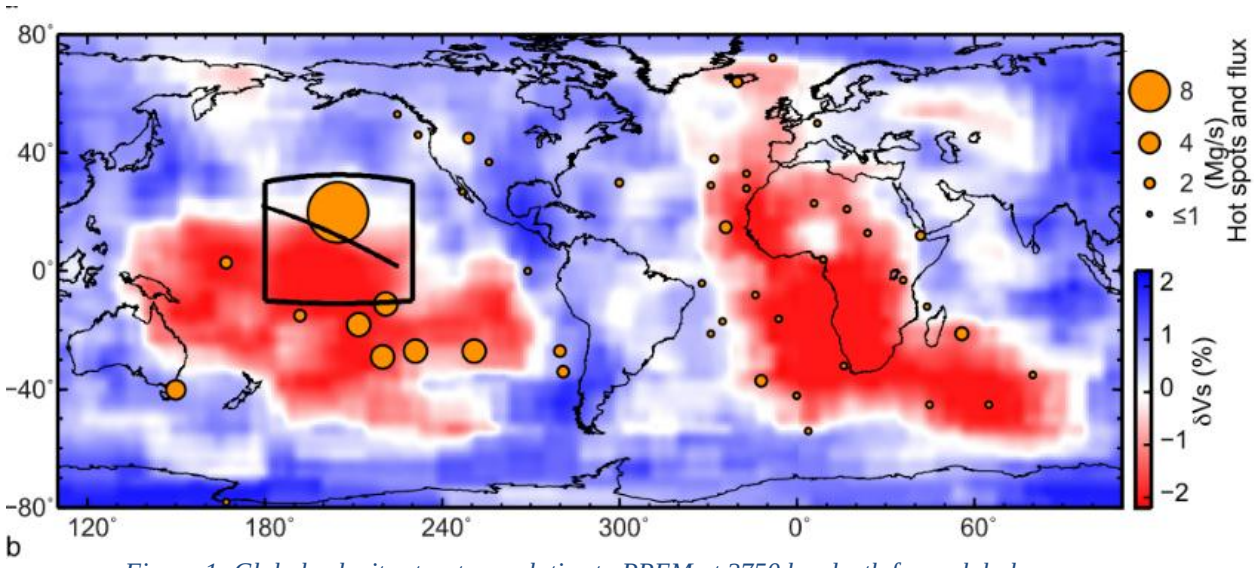

Figure 1: Global velocity structure relative to PREM at 2750 km depth from global tomography model TXBW (Grand, 2002) with hotspot locations scaled by flux in megagrams per second (Sleep, 1990). TXBW was constructed using travel times of SS and ScS multibounce phases. Red regions denote negative shear wave anomalies and define LLVP borders (Zhao et al., 2015).

Insights into LLVP behavior originally stemmed from geographic correlation with hotspot volcanism and mantle plumes (e.g., Burke and Torsvik, 2004). The geochemical signatures of ocean island basalts erupted at these correlated hotspot volcanoes show enrichment in primordial

components, such as ^{3}He, not observed at non-correlated hotspots (Williams et al., 2019). This hotspot correlation (Fig. 1) and seismic evidence of sharp boundaries lead researchers to interpret LLVPs as both thermally and compositionally distinct plumes that feed surface volcanism (McNamara and Zhong, 2004, 2005; Zhao et al., 2015). This interpretation implies that LLVPs are long-lived thermochemical reservoirs that can generate plume behavior in the surrounding mantle. For LLVPs to be both hotter than the surrounding mantle and long-lived, they must be composed of material of inherently higher density than the ambient mantle (e.g., Kellogg et al. 1999). The actual density of the LLVPs remains debated, with evidence in favor of denser-than-average LLVPs coming from normal mode splitting (e.g. Ishii and Tromp, 1999, 2001; Moulik et al., 2016) and tidal constraints (Lau et al., 2017), and evidence in favor of lighter-than-average LLVPs coming from Stoneley mode measurements (Koelemeijer et al., 2017). Higher resolution topography of LLVPs revealed grouped plumes of actively upwelling material enriched in high-density material (French and Romanowicz, 2015). Davaille and Romanowicz (2020) interpret these models to imply that LLVPs are changing over time and mixing with the surrounding mantle. These results are supported by recent geodynamic models that show upwelling plumes with LLVP characteristics can be stable for over one billion years (Liu et al, 2024). Evidence against the plume model came from a recent paper that concluded 1-2 orders of magnitude grain size increase in LLVPs compared to the surrounding mantle (Talavera-Soza et al., 2025). Upwelling and mixing reduce grain sizes, meaning LLVPs would need to be stagnant for billions of years to achieve cm-scale grains (Liu et al. 2024).

The inability to agree on LLVP behavior and properties in the present-day mantle creates difficulty in understanding their possible origins. Primordial explanations for LLVPs include remnants of Theia or early crystallization of the Hadean magma ocean (Yuan et al., 2023; Lee et al., 2010). Some interpretations view LLVPs as more recent; formed from sunken oceanic crustal slabs or core-mantle mass transfer (Tackley, 2012). Currently, all these interpretations have geophysical evidence to support them. The primordial origin hypotheses are backed by models that predict large grain sizes in LLVPs as long-lived stability is required for large grains to grow. The relationship between OIBs and LLVPs is an unreliable estimate of LLVP age because present-day core-mantle exchange could produce non-ancient LLVPs with primordial signatures. The stability of these regions over billions of years can be explained by viscosity differences induced by elevated grain sizes and the rotation of the earth stabilizing antipodal high-density regions (Liu et al., 2024). The crustal slab interpretation comes from the analysis of LLVP boundaries indicating sharp edges and a density contrast. Crustal slabs are denser than the mantle and could, therefore, sink to the core-mantle boundary. Recent models show subduction zone history over the last one billion years could naturally create antipodal LLVPs (Panton et al., 2025). If the differences between LLVPs and the surrounding mantle were purely thermal, LLVPs would be buoyant. LLVPs must differ from the surrounding mantle in more complicated ways than purely thermal. Seismic velocity alone cannot separate thermal, density, and viscosity effects from each other, but by incorporating attenuation stronger constraints can be calculated on the source of heterogeneity.

Seismic Attenuation

As they travel through the Earth, seismic waves experience energy loss resulting from microscopic dissipative mechanisms occurring across a range of timescales (for a recent review, see Romanowicz and Mitchell, 2015). The mechanisms convert the stress added by seismic

waves into strain within a system in the form of anelastic (non-reversible) behavior. These are typically parameterized by the dimensionless quantity Q, called the quality factor, which tracks the fraction of energy lost per cycle of oscillation: $Q = 2\pi E/\Delta E$.

Anelastic attenuation can be related to material properties and ambient conditions through an Arrhenius-type equation (Eq. 1):

$$Q = Q_0 \exp\left(\frac{\alpha H^*}{RT}\right)$$

Equation 1: Quality factor (Q) has an exponential relationship with temperature(T), enthalpy (H), and the frequency-dependence of attenuation (α) and a linear relationship with Q_0.*

wherein Q is the quality factor, the inverse of attenuation and a measure of how much energy a wave loses per cycle of oscillation, R is the ideal gas constant, H^* is the activation enthalpy of the materials, and α is the frequency dependence (Anderson and Given, 1982). Activation enthalpy (H^*) represents the energy barrier for a relaxation process (e.g., vacancy formation, dislocation creep, thermoelastic internal friction). This value is dependent on the concentration of impurities and physical defects in the system. Materials absorb waves at preferred wavelengths; α is a coefficient that describes the relationship between the frequency content of the wave and the variation of Q with frequency. Finally, Q_0 is a pre-exponential term that accounts for a wide variety of material properties that have varying influence on attenuation including volatile content, density, and grain size. Definitions and estimates of Q_0 within the Earth vary greatly, however, it acts as a scalar quantity for model correction. Contributions to Q_0 from volatile content can be ignored as lower mantle minerals are thought to contain less than 50 ppm (by wt.%) H_2O (Liu et al., 2021). The primary mechanisms for anelastic behavior in the mantle are dislocation creep, grain boundary sliding, and diffusion creep (Jackson and Anderson, 1970). These grain interactions are primarily a function of grain size, and therefore grain size is the controlling factor for the pre-exponential term in the lower mantle. Q is exponentially related to the inverse of temperature, so as T increases the quality factor will exponentially decrease and attenuation will exponentially increase.

As a seismic wave propagates through a material, stress and strain vary over time. This can cause individual grains to slide past each other and defects in crystals to migrate removing energy from the wave. The easier it is for a material to deform; the more anelastic attenuation the wave experiences. In high-temperature systems, more energy is lost to the travel medium through grain sliding and defect migration. Elevated temperature is the standard explanation for LLVP heterogeneity as elevated temperatures slow seismic waves by decreasing density and rigidity. In most regions of the mantle, elevated temperatures denote slower waves and higher attenuation, however, substantial changes in the material parameter (Q_0) can disrupt this relationship. Material chemistry, density, and temperature vary with location within the Earth. The Q value, and therefore attenuation, will change in response to these parameters. A seismic wave will pass through regions with varied attenuation before the signal is observed at the receiver. The total attenuation a wave experiences over its path can be expressed as t*, the anelastic delay time. This value integrates the total energy lost over the wave path. Attenuation spreads the frequency content of a wave and causes a delay between when peaks arrive. This delay time is the primary source of information

used in this paper to view attenuation differences. The equation that describes t* (Eq. 2) is an integration of the attenuation at a point with respect to the duration in that region.

$$t^* = \int_{path} \frac{1}{Q(\vec{x})} dt$$

Equation 2: Anelastic delay time (t) is the integration of attenuation at a given location as it changes with position with respect to time.*

The anelastic delay time is sensitive to both the attenuation in a region and the time spent at that point. This integration can be made discrete, where an average *Q* is calculated for a region and summed with respect to the time spent in that region. In contrast to inelastic attenuation, extrinsic attenuation is the loss of wave energy by scattering or spreading. Extrinsic attenuation is an unrelated phenomenon, with no relationship to *Q*, which yields the same result of decreasing the amplitude of the wave at the receiver. Geometric spreading reduces amplitude as the energy from a wave arrives at multiple points spread over an area of the Earth. This is corrected for in the Lai and Garnero (2020; 2019) datasets using virtual seismograms that correct for broadening waves through seismogram stacking. Scattering occurs when differences in structure that a wave interacts with are similar in size to its wavelength. This causes focusing and defocusing of the wave in ways that can produce constructive or destructive interference. It can be difficult to distinguish between scattering and anelastic attenuation as they both produce delay times and amplitude changes.

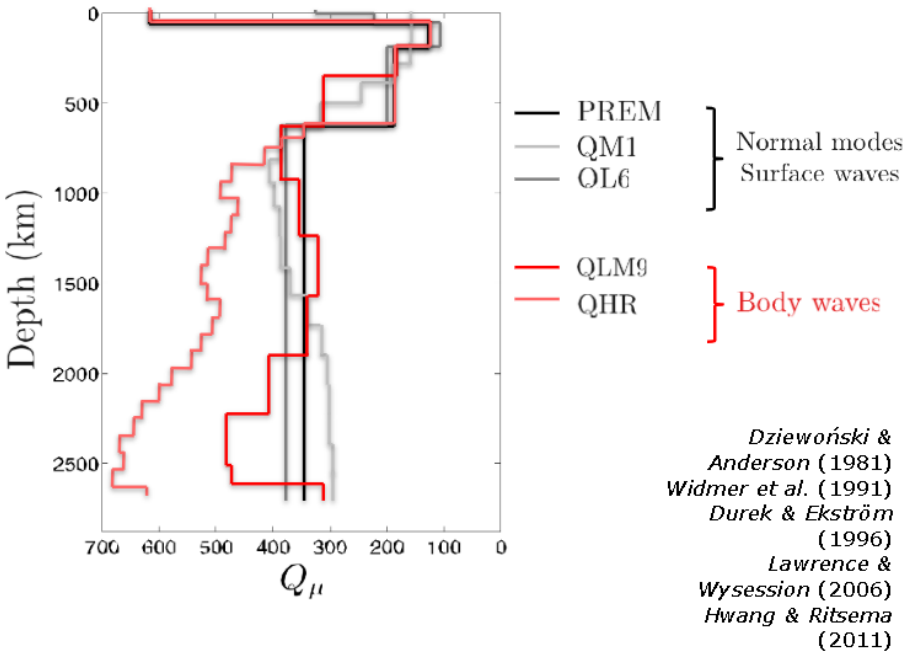

Figure 2: Compilation of 1D attenuation models from the surface to 2800 km for normal mode and body wave measures. QLM9 is the 1D results from the most widely known global 3D attenuation map. Attenuation jump at the bottommost mantle is a result of the D" discontinuity phase transition from perovskite to post-perovskite (Matas and Bukowinski, 2007).

Attenuation within the Earth varies with depth, surface location, and wave type. Figure 2 shows that the upper mantle attenuation is agreed upon down to the 410 km discontinuity. The upper mantle has a lower quality factor for all waves than the lower mantle, thus a sizable portion of attenuation shown in waveform measures is accumulated in the upper mantle. It shows body waves, the focus of this study, in red. The Q value of body waves in QLM9 is lower than the PREM model for surface and normal waves. Body waves travel through the interior of the planet and often at a higher frequency than normal modes and surface waves. Surface waves travel along the surface of the planet and at long periods, can circle the entire globe to create normal modes. The increased quality factor in measurements conducted using body waves is likely indicative of the frequency dependence of attenuation within the Earth. Attenuation is proportional to a power law function, $Q \propto Q_0 f^{\alpha}$, where f is the frequency and α the frequency dependence of the material at that frequency; thought to be around 0.1-0.3 in the mantle (Lekic et al. 2009). High-frequency body waves are not as affected by per-cycle attenuation in the currently accepted absorption band of the mantle, but they are affected more by attenuation overall because the number of oscillations increases more rapidly than the per-cycle attenuation decreases with frequency. These increase the anelastic delay time to a greater extent than observable in normal modes. Additionally, body waves are of particular use in this study because they can sample deep mantle structures, including LLVP regions. Surface waves have a maximum effective sampling depth between one-half and one-third the wavelength of the wave. High-frequency surface waves penetrate shallowly and are unusable for deep mantle imaging.

Motivations

The appeal of characterizing LLVPs connects to geochemistry, planetary geology, and seismology. There are many questions surrounding LLVPs, including their origin, history, and composition. Seismic measurements of the lower mantle are obstructed by the overlying structures of the crust and upper mantle. Seismic surveys conducted on LLVPs have focused on their characteristic velocity drop and mapping where they occur. Although this is useful in understanding how seismic data are distorted, it does not reveal much about the structures themselves. Characterizations of the physical properties of LLVPs provide better constraints on when they developed and how they interact with the mantle in the present day.

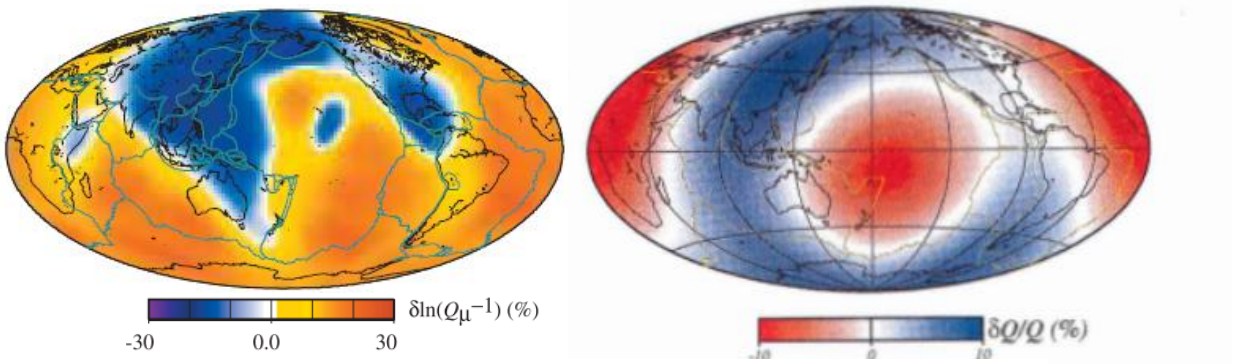

Figure 3: Lateral attenuation map at 2800 km for a body wave study and preliminary waveform matching study, respectively (Lawerence and Wysession, 2006; Romanowicz, 1998). QLM9 was constructed using t and Q Model degree 2 was constructed using waveform matching. Blue regions in both represent low attenuating regions.*

There have not been many models made of lower mantle attenuation. Two relevant models exist: one published based on t* measures (QLM9) and an unpublished model from a review paper on lower mantle attenuation (Lawrence and Wysession, 2006; Romanowicz, 1998). These models are low resolution but retrieve similar patterns of the attenuation structure near the core-mantle boundary. As seen in Fig. 3, these models resolve higher relative attenuation in regions that would now be considered LLVPs (Central Pacific and Africa). QLM9 (left) was constructed using body wave measures and the Romanowicz (1998) model (right) was constructed using waveform matching. The main disagreement between these models is the amplitude of the attenuation. These models use waves of different frequencies, so any potential frequency dependence of attenuation can map into differences between the models. Nevertheless, the spatial patterns of attenuation mapped in the two models are consistent with a thermally dominated explanation for both velocity and attenuation contrasts, because high temperatures will decrease seismic velocity and increase attenuation.

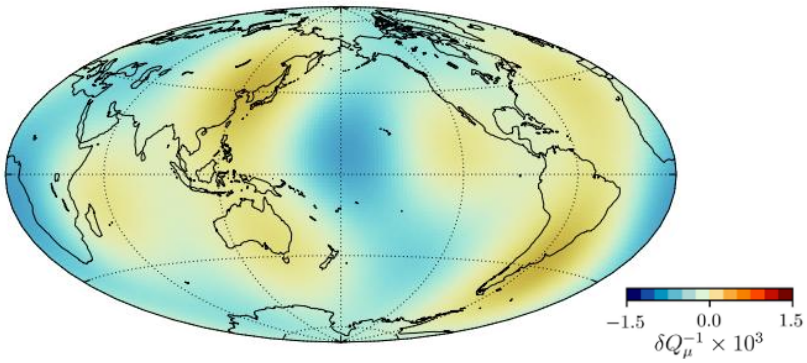

Figure 4: Attenuation model for QL3S4 plotted at 2400 km depth. Shows relative attenuation in LLVPs opposite to that from two previous models. (Talavera-Soza et al., 2025).

Recently, a new model, QL3S4, based on the analysis of normal mode anelastic splitting functions (Talavera-Soza et al., 2025) was published that is in complete disagreement with the previous studies. This model has lower attenuation in LLVPs than in the surrounding mantle. This is in contrast to the upper mantle, where the QL3S4 reveals attenuation variations that are anticorrelated with V_S behavior consistent with a thermal origin for both. Toward the base of the lower mantle, at 2400 km depth, this relationship breaks down. Here, QL3S4 recovers low-velocity zones to be correlated with low attenuation, challenging traditional views of the dominant role of temperature for both parameters. Therefore, QL3S4 motivates deep Earth scientists to consider alternative explanations for attenuation in LLVPs besides thermally controlled anelasticity. Talavera-Soza et al. (2025) argue that LLVPs not only have elevated temperatures (450-500 K hotter from the ambient mantle) but also much larger grain size, 10^{-2} m compared to 10^{-5} m in the surrounding mantle. If grain size variations play an important role in explaining lower mantle heterogeneity, they would also have profound implications for the viscosity of LLVPs and their mixing. This is because convection is expected to be a destructive process that would restrict grains from reaching cm-scale features. Additionally, large grain sizes imply high-viscosity resistance to flow. Therefore, if QL3S4 is correct, LLVPs would be ancient, long-lived, high-stability regions that do not vigorously convect internally and remain unmixed with the surrounding mantle.

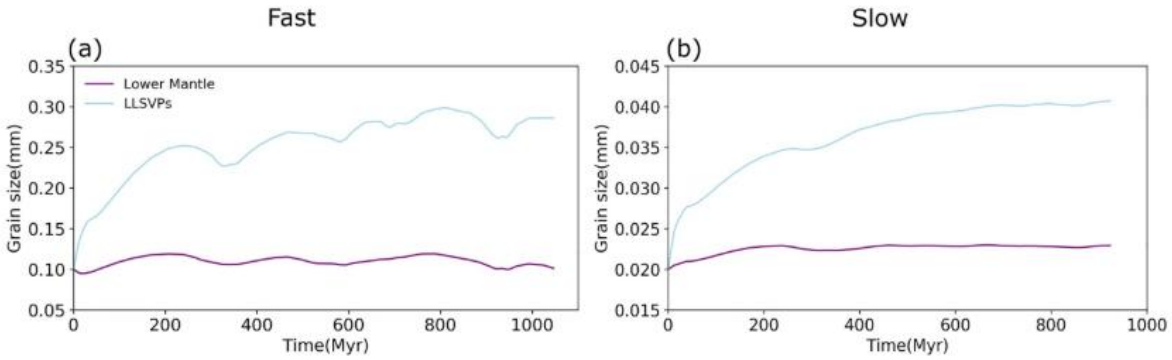

Figure 5: Modeled LLVP grain size compared to surrounding lower mantle for different grain growth rates projected from 0-1000 million years (Liu et al., 2024).

Liu et al. (2024) conduct geodynamical simulations that compare different rates of grain growth and destruction to examine LLVP plume behavior over long timescales. They find that grain size variations enhance plume stability for up to one billion years. Modeled results show that plumes can remain stable for the entirety of the model study time (1 Ga), the upper limit of grain sizes achieved by this model in LLVPs is 0.4 mm, an equilibrium grain size in LLVPs of around twice that of the lower mantle. This is substantially lower than the 10-100x increase in the Talavera-Soza et al. (2025) model (Fig. 5). The equilibrium model allows for grain growth by diffusion creep and grain reduction by dislocation creep. Elevated temperatures both increase grain growth and grain reduction; thus, cm scale grains cannot be achieved in an LLVP that experiences dislocation creep. Even in the model that does not include grain destruction, grain sizes only achieve a peak diameter of 0.5 mm.

Questions about LLVP's origin and role in mantle dynamics cannot be answered without accurate models of geophysical properties. There is currently disagreement on whether LLVPs are higher or lower attenuating the lower mantle. While there is agreement that LLVPs are likely hotter than the lower mantle with larger grain sizes, there is disagreement on which has the dominant effect on attenuation in the lower mantle. Constraining the relative attenuation of LLVPs will provide insight into the relative temperature and grain size characteristics of the lower mantle. This information allows for the refinement of geophysical models to predict more accurately how long LLVPs have been present at the CMB and the degree of interaction they retain with the ambient mantle.

Hypotheses

To begin to constrain these relative attenuations to answer this question, the following hypotheses were developed. The null hypothesis of the proposed study is that LLVPs have no significant effect on the attenuation of shear waves passing through them. This would be supported if no correlation is found between attenuation experienced by waves and the time they spend traversing the LLVPs. The first alternative hypothesis suggests that LLVPs are heterogeneous compared to the ambient lower mantle, primarily due to temperature differences. This would be supported if waves that travel through LLVPs show higher attenuation, particularly if they become more attenuated the more time within these regions. The second alternative hypothesis suggests that grain size is the controlling factor of attenuation within LLVPs. This would be supported if waves passing through LLVPs show lower attenuation compared to those traveling through other mantle regions.

Methods and Data

The data for this project comes from Lai and Garnero (2020) and Lai et al. (2019). These two datasets combined provide 35,300 S waves and 7,015 ScS waves containing t* data along with SS and ScS multibounce phases for additional investigation. The paths taken by these waves are compared to a vote map of LLVP latitude, longitude, and depth from Cottaar and Lekic (2016) in order to compute the total travel time spent by the waves in LLVPs. The vote map shows the location of LLVPs as determined by five separate tomographic models (Fig. 6). Each model counts as a vote for a perceived LLVP location by latitude, longitude, and depth. The regions where more models agree are given more votes, ranging from zero to five. This vote map allows us to decide how conservative or liberal we are in determining LLVP boundaries. A majority agreement of 3 votes was selected to balance data availability and certainty based on the results of the first method.

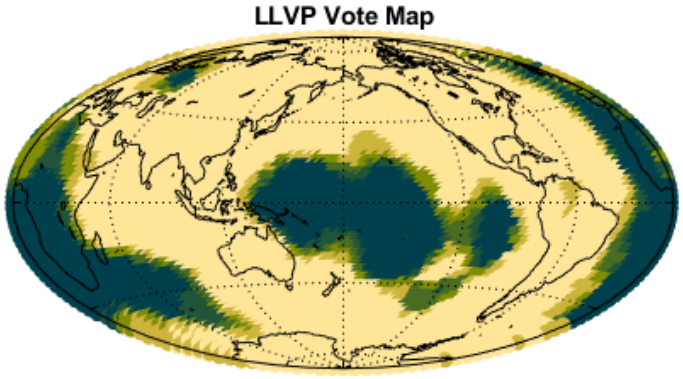

Figure 6: LLVP Vote Map at 2700 km depth ranging from 0 to 5 represented with increasing darkness. The Perm, Russia anomaly is recorded as an LLVP location along with Jason and Tuzo (Cottaar and Lekic, 2016).

The upper mantle is known to be more highly attenuating and variable than the lower mantle; for example, in the PREM model, the upper mantle is 4-5x more attenuating than the lower mantle (Dziewoński and Anderson, 1981). The paths waves take through upper mantle structures, and how long they spend traversing them, could affect the measured t* values in ways that do not relate to LLVP properties. This project used two distinct approaches for accounting for upper mantle attenuation signals: S-ScS t* differential and corrections based on two published models of upper mantle attenuation. The first analytical method pairs waves that have similar source and receiver locations, but different paths through the lower mantle to view differences in attenuation with depth. Figure 7 shows the underlying principle behind the method. ScS waves bounce off the outer core before returning to the surface so they will sample different depths than a S wave. This bounce point has a consistent depth for all ScS waves and allows for certainty in sampling location. The paths taken through the upper mantle change in similarity as the epicentral distance changes. Paired S and ScS waves with epicentral distances ranging from 50-80 degrees were chosen for this method to ensure similarity in the upper 500 km of the mantle without being overly similar in the lower mantle. More S waves than ScS produced at seismic events; ScS wave availability is the primary limiting factor of this method. To ensure

unique location data when multiple S waves were assigned to the same ScS wave, one was randomly assigned to be the value.

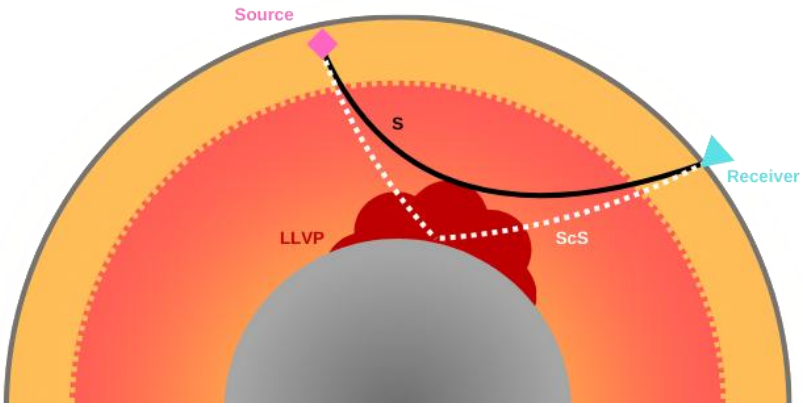

Figure 7: Diagram of S and ScS similarity in the mantle. The yellow section represents the mantle transition zone where the LLVPs have no effect on t. The ScS wave (white) samples the lowermost mantle by reflecting off the outer core while the S wave (black) samples the mid-mantle.*

Subtracting the t* value of the S wave from the t* value of the ScS wave with the same source and receiver provides the deviation of accumulated attenuation in the lower mantle. For paired S and ScS waves traveling through a uniform medium, the ScS wave will travel a greater distance and would show a higher t* and therefore positive ScS-S δt*. A ScS-S δt* value below 0 shows that the ScS wave experienced a zone of low attenuation. These differential t* measurements are then sorted by both sampling location and time spent in LLVPs. The bounce points of the ScS waves are compared to the LLVP vote map (Fig. 8) and sorted into histograms of differential t* for increasing strictness of LLVP definitions.

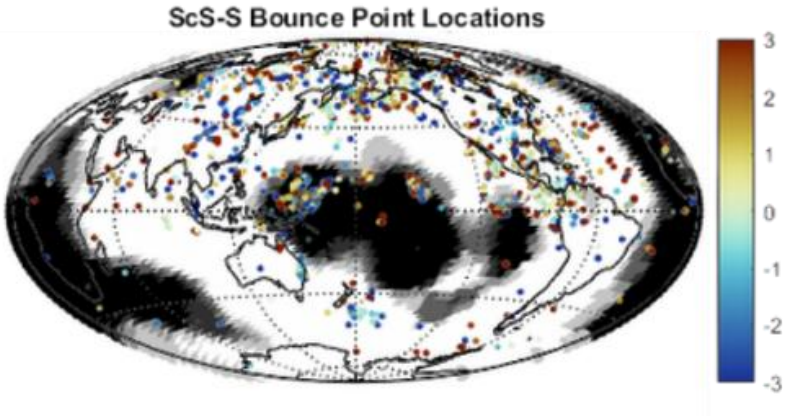

Figure 8: ScS bounce point locations for waves with corresponding S waves matched to source and receiver locations with epicentral distances between 50 and 80 degrees. This produces 2,304 data points and 480 points where at least three models agree an LLVP is. The scalebar is ScS-S δt, higher values indicate a lower attenuating lower mantle.*

Next, the ray paths are calculated to determine the time spent in each region of the mantle to view differences more accurately in t*. This method was conducted using S waves exclusively

because they are geographically widespread and sample many depth ranges in the mantle. These waves are then compared to two published upper mantle attenuation models: SEMUCB-UMQ (Karaoğlu and Romanowicz, 2018) and QFRSI12 (Dalton et al., 2008). The S waves from the provided datasets have a source location and receiver location. This information is input in TauP toolkit which calculates travel times and turning points based on the PREM velocity model (Crotwell et al., 1999). With the path information from TauP Toolkit, the wave location for latitude, longitude, and depth is calculated along with the total time the wave has been traveling. These continuous data can be divided into point counts with respect to time. The path is interpolated over 0.1 second intervals and the position at each interval is recorded.

These paths can be related to a spherical model of the Earth divided into voxels with specific characteristics. Each voxel is a 3-dimensional object to represent a specific area and volume within the Earth. These voxels contain information on the location of the voxel, the number of votes for an LLVP at that location, and the velocity given by PREM. The creation of a voxelized Earth necessitates a conversion of the t* integration to a discretized summation (Eq. 3).

$$t^* = \sum_j \frac{1}{Q_j} \Delta t_j$$

Equation 3: Discretized anelastic delay time (t) formula is a summation of attenuation accumulated in a specific region summed over the time spent within that region. Each voxel exists as a region (j) that has an associated Q value and wave duration, these values are used to calculate a predicted t*.*

Any voxel within a region where data exists in the upper mantle map is also set to the *Q* of the model at that location. The *Q* for all regions outside the model space is set at 10,000 to provide minimal contributions to t*. Given the *Q* value in each region and the time spent in each voxel, obtained by TauP, a predicted t* value is calculated. The corrected t* is the difference between the calculated t* and the observed. At this point the corrected t* shows all attenuation not accounted for in the upper mantle. The relationship between time and t* is linear, assuming a constant attenuation (Jackson and Anderson, 1970). The slope of the relationship between the corrected t* and time shows the average attenuation in the lower mantle. This value was calculated to be 558 and 543 for each model. These *Q* values fall within the range of the 1D *Q* models for body waves shown in Figure 2. These attenuation values are then assigned to voxels outside the model space as an average value of lower mantle attenuation. The new calculated t* is based on the upper mantle model and a calculated average lower mantle *Q*. This predicted t* for waves assumes an undisturbed path through the mantle that accumulates variable attenuation in the upper 660 km and a constant attenuation in the lower mantle. Any deviations from the predicted t* are assumed to represent tomographic features in the lower mantle, including LLVPs. Comparing the relationship between predicted t* and observed t* for time spent in LLVP compared to total travel time displays whether LLVPs have a positive or negative differential *Q* compared to the ambient lower mantle. This method allows for a more direct measure of the effect of LLVPs on the wave because it allows for a calculation of time spent in LLVPs. Anelastic delay time is integrated with respect to time, therefore the duration spent within LLVPs should represent the primary controlling factor if there is a difference in *Q* between LLVPs and the ambient lower mantle. It also has greater coverage due to not being limited by ScS availability (Fig. 9).

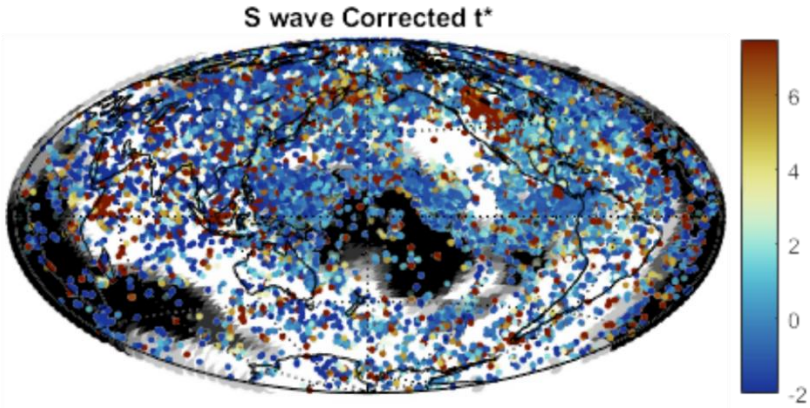

Figure 9: S wave turning point locations provide more robust coverage. The dataset contains 35,297 usable values for S wave data with depths ranging from 770 km to 2890 km. The colorbar represents corrected t values based on SEMUCB. Positive values show a higher observed attenuation than predicted attenuation.*

Results

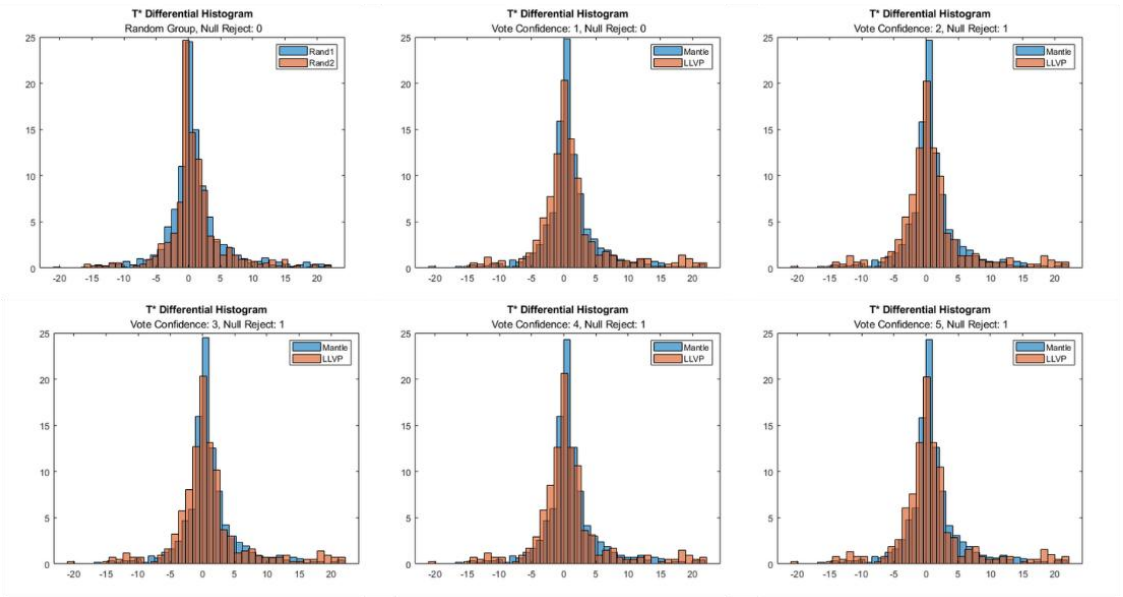

Figure 10: ScS-S δt histograms for random selection and LLVP vs lower mantle model agreement from 1 to 5. Histograms have 40 bins and are normalized to the percentage of data in each bin. The random group and minimum agreement models accept the null hypothesis and display identical distributions. Model agreement 2 to 5 reject the null according to the Mann-Whitney U test.*

In Fig. 8, the ScS-S δt* measurements are plotted at the ScS bounce point. No clear relationship can be observed between the δt* values and LLVP location. However, when examined as histograms, shown in Fig. 10 the distribution patterns are non-identical. The distributions of t* for waves that do and do not interact with LLVPs for increasing model certainty were compared with the Mann-Whitney U test. This test was chosen because ScS-S δt* is not normally distributed.

A non-parametric statistical test can compare two non-gaussian distributions in relation to a null hypothesis wherein the distributions are identical. The random selection group had an identical distribution, as expected, and so did the minimum agreement vote count (Fig. 10). The remaining vote levels rejected the null hypothesis and were statistically different between assigned groups. This showed that the LLVP locations had a significant effect on the distribution of ScS-S δt*. Additionally, one vote for "slow" was not strict enough to be reliably used as an LLVP indicator. The results of the ScS-S method support the use of a majority agreement for LLVP locations by the path correction method.

The ScS-S δt* method had limited interpretation viability because of a lack of data availability. The combined datasets had 7,015 ScS waves with S waves matching source and receiver locations, wherein both waves have t* measurements provided. After filtering for epicentral distances between 50 and 80 degrees only 2,304 pairs remained. Comparing the LLVP vote map to the bounce points of the ScS waves revealed only 434 waves where the bounce point sampled a location that most models agree is an LLVP. When analyzing the median δt* values within bins of time the ScS wave spent in LLVP, most bins have less than a statistically significant number of waves (count < 35). The data from the path correction method displayed large amounts of variance, which is common in t* measures due to interference between ScS and S waves that can cause up to 1.5 s uncertainty in anelastic delay time (t*; Bhattacharya et al., 1996). The error from scatter and ScS and S interference invokes the need for larger datasets to compensate for obscured signals. The ScS-S method was useful for showing a statistically significant difference between attenuation in LLVPs compared to the surrounding mantle. High variance and low sampling density made it unrealistic to attempt to draw conclusions about how LLVPs vary from the mantle from this approach.

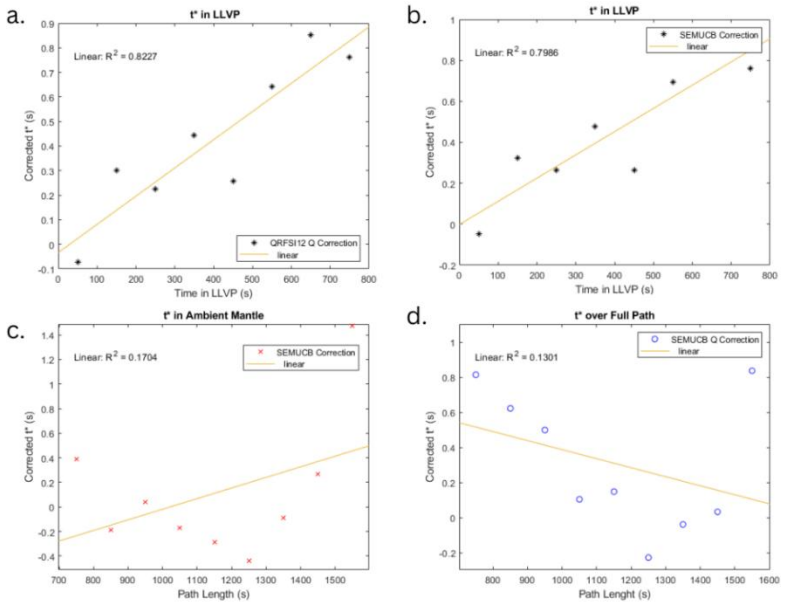

Figure 11: Corrected t values plotted against time spent in LLVPs for QRFSI12 (a.) and SEMUCB (b.) models. Corrected t* compared to time spent outside of LLVPs(c.) and total path length (d.) for the SEMUCB correction. The latter have no correlation.*

The second method covered many of the shortcomings of data interpretation involved with ScS-S measurements. Path calculation expanded the available data from 2,304 paired waves to 35,297 unpaired S waves. The data were binned in intervals of 100 s for which non-sparse data existed. The median corrected t* in these bins displayed a positive relationship with time spent in LLVPs (Fig. 11a, Fig. 11b). The values are largely above zero, meaning the observed t* value is larger than the t* value calculated based on an average lower mantle attenuation. Additionally, the difference in observed and predicted t* grows with time spent in LLVPs. Travel time in a region with a *Q* lower (higher attenuation) than the calculated average *Q* of 558-543 would increase the t* observed compared to the predicted values. Time spent in LLVPs has the highest correlation with variations from the calculated model results (R^2 = 0.8227; 0.7986). This relationship is not observed with total travel time for all waves or travel time for waves that never interact with LLVPs (Fig. 11c, Fig. 11d). The anelastic delay also increases as the total wave travel time increase, however, it does not change the t* systematically from the predicted values. Corrected anelastic delay time and path length are poorly correlated for all waves (R^2 = 0.1301) and waves that never interact with LLVPs (R^2 = 0.1704). The positive trend in deviations from the predicted and observed t* values is not explained by travel time exclusively.

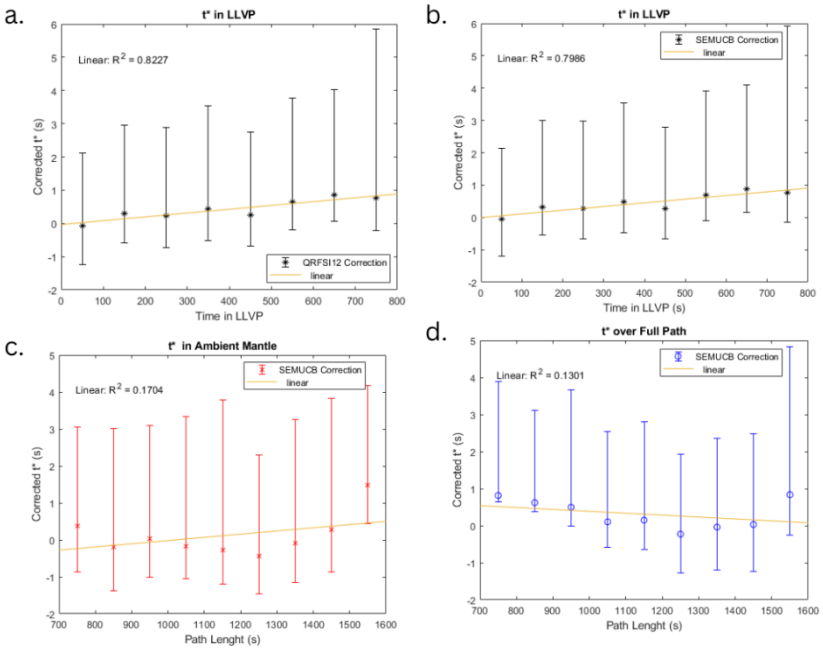

Figure 12: (upper) Figure 11: Corrected t values plotted against time spent in LLVPs for QRFSI12 (a.) and SEMUCB (b.) models. Corrected t* compared to time spent outside of LLVPs(c.) and total path length (d.) for the SEMUCB correction. Error bars are the 25th and 75th percentile quadrants for binned data.*

The two models, when applied to this method, had similar variance reductions of 1.46% and 1.41%; the R^2 was slightly higher using QRFSI12 (R^2 = 0.8227) than SEMUCB (R^2 = 0.7986). The error is reported as the upper and lower quartile ranges for bootstrapped means within bins

(Fig. 12). The variance of the quartile ranges is greater than the range of median values. The remaining uncertainty on these data is because we do not correct for inelastic attenuation due to scattering and defocusing. Scattering-based attenuation affects all waves in the compiled datasets; therefore, it was ignored due to the volume of measurements provided by this method. Scattering can produce attenuation signals greater than that of attenuation and likely represent much of the signal we see (Chaves et al. 2016). This is the same source of error that made the ScS-S method unreliable for quantifying the relationship between t* and LLVPs, however, the addition of over an order of magnitude more data allows the median values to be more credible. The ScS-S method, when sorted in 6 bins by time spent in LLVPs between 0-500 seconds, yielded around 260 values per bin. The path correction method when sorted in 8 bins for time in LLVPs between 0 and 800 seconds yielded an average of 2,800 values per bin. Large datasets should show enough random errors that the medians are statistically significant despite large uncertainty. These methods together have led me to conclude that for body waves, LLVPs are higher attenuating than the surrounding mantle.

Discussion

The results of this study are comparable to the older models of lower mantle attenuation (Lawrence and Wysession, 2006; Romanowicz, 1998). QLM9 was constructed using the same data type as this study, t* measures of body waves. At the base of the mantle, QLM9 resolves high attenuation under the Central Pacific and Africa. This agrees with the positive correlation between t* and time in LLVPs observed in this study. Similarly, the results are consistent with the pattern of attenuation obtained by Romanowicz (1998).

The results of this study do not agree with QS4L3, the model that depicts lower relative attenuation in LLVPs. QS4L3 was constructed using long-period normal modes. The two possible explanations for the disagreement between this model and the findings of this study are that approximations made in the construction of QS4L3 greatly affect measured attenuation in the lower mantle, or the frequency dependence of the lower mantle causes short and long period waves to behave differently in LLVPs. The main approximation in QS4L3 is the self-coupling approximation. In this approximation, normal modes are isolated and only interact with themselves. In actuality, modes of different degrees and orders can leak energy into nearby modes, thereby altering the observed splitting. This assumption limits the model to only resolving even degree structure. This alone is not enough to explain the deviations from QLM9 because Romanowicz (1998) shows degree 2 structure in agreement with QLM9. Additionally, QS4L3 is unable to recover any structure in the bottom 400 km of the mantle. If the high attenuating portion of LLVPs is below 2400 km then QS4L3 could resolve a different structure compared to the other models at 2800 km. Aside from approximations taken in the construction of QS4L3, a misunderstanding of the frequency dependence of lower mantle materials could influence the discrepancies between these models.

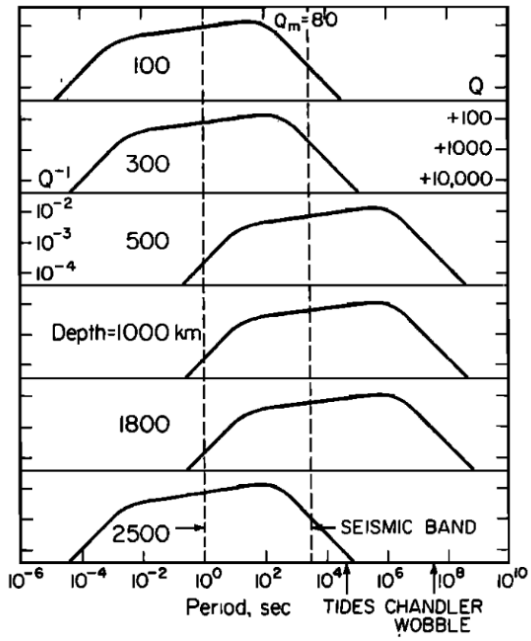

Figure 13: Frequency domain location of the absorption band of the mantle at increasing depths in the Earth. Absorption band shifts to favor low-frequency waves with depth in the Earth apart from the D" layer. (Anderson and Given, 1982)

All materials have an absorption band. The absorption band represents frequencies that are most highly attenuated by the material. The frequency dependence of attenuation is based on the absorption band of the material and the frequency of the wave that samples it. The frequency dependence (a) is considered constant or slightly increasing (0.1-0.3) within the absorption band and close to 1 beyond the corner frequency (Anderson and Given, 1982). The corner frequency represents the upper and lower limits of efficiently attenuable frequencies of a material. Beyond the corner frequency, attenuation is reduced and no longer has any dependence on frequency. The seismic band noted in Figure 13 is the usual frequency range of seismicity within the Earth. The seismic band at 2500 km is shifted and has lowered absorption around 10^3 s periods. However, at 1800 km the 10^3 s period wave has higher absorption compared to low-frequency waves. The corner frequency is at opposite ends of the seismic band (body waves vs normal modes) at depth. If the LLVP material has an absorption band that primarily attenuates high-frequency waves such as post-perovskite then it could show both high attenuating signal for body waves, seen in QLM9, and lower attenuation for long-period normal waves, seen in QS4L3. A change in the absorption band between LLVP material and the surrounding mantle is another explanation for the discrepancy between our results. The preliminary results from Romanowicz (1998) agree with QLM9 despite being constructed using long-period waveforms. The waveforms used in Romanowicz (1998) are relatively short periods compared to the ones used to construct QS4L3, landing on the 10^2 s period portion of the absorption band. These signals predict the same relative attenuation as body waves.

It is entirely possible that both the results of this study and QS4L3 are valid. The addition of a possible absorption band shift within LLVPs complicates attenuation studies in new ways.

Future studies on attenuation should aim to compare the frequency dependence of waves in LLVPs and the selection of a frequency that maintains similar absorption band peaks throughout the lower mantle. Without deconvolving the effects of frequency, seismology cannot be used to define physical properties in the lower mantle.

Conclusion

The results of this study show a link between increased attenuation and LLVP location. The difference in observed and predicted t* increases according to time spent in LLVPs. This high attenuating relationship is interpreted as a high temperature, low viscosity LLVP material. The null hypothesis of no relation between attenuation has been falsified by the results of the differential ScS-S method. Additionally, the hypothesis of lower attenuation within LLVPs is not supported by the results of the path correction method. There is not enough information to falsify this hypothesis without additional information on how the frequency content of waves effect attenuation with LLVPs. The results of this study can be used to conclude that for body waves, LLVPs are higher attenuating than the surrounding mantle. The presence of high attenuation in LLVPs has implications for the interpretation of present-day LLVP behavior and their possible origin. As temperature increases, attenuation increases exponentially. Increased temperatures also increase grain growth rates. In a high attenuating LLVP, grain destruction must be present to reduce the attenuation-decreasing effect of cm-scale grains. Grain reduction relates to readily convecting LLVPs either internally or through mixing with the mantle. Thermally dominated anelasticity supports the superplume hypothesis, in which LLVPs are substantially hotter than the ambient mantle and change shape over time. This temperature increase could be a result of an enrichment in primordial heat-producing isotopes (Guerrero et al., 2024). Possible LLVP origins that include heat-producing elements are Theia impactor remnants, early magma ocean crystallization, or core-mantle mass transfer. The sunken oceanic slab interpretation of LLVPs would likely produce high rigidity, low temperature LLVPs and is not supported by this study. Future applications for these results must consider that the frequency content of waves used to examine the lower mantle may greatly affect the observed attenuation.

Acknowledgments

Thank you to Prof. Ved Lekic for advising me through this study and assisting me where either my seismological or mathematical foundation was lacking. Thanks to Brenna Henderson, Sami Toibero, Ashley Hanna and other members of the Maryland Seismology lab for assisting me with developing presentations. Thanks to Prof. Barbara Romanowicz and Prof. Colleen Dalton for providing access to their attenuation models for this study. Finally, I would like to thank Peter B. Stifel, whose Senior Thesis Endowment allowed me to present my research at the Seismological Society of America Annual Meeting 2025.

Appendix A

All codes and datasets to produce the plots detailed in the paper can be found at the following dropbox:

https://www.dropbox.com/scl/fo/eshsjlaqrqccnsfrm13r3/AAmRqxpbnD7dZPQhvcw3QkE?rlkey=0euh8uxsum5bbkqu8tzd3gsh6&st=0u21tnyo&dl=0

Appendix B

I pledge on my honor that I have not given or received any unauthorized assistance on this assessment.

Bibliography

Anderson, D. L., & Given, J. W. (1982). Absorption band Q model for the Earth. *Journal of Geophysical Research: Solid Earth—Wiley Online Library*, *87*(B5), 3893-3904. https://agupubs.onlinelibrary.wiley.com/doi/10.1029/JB087iB05p03893

Bhattacharyya, J., Masters, G., & Shearer, P. (1996). Global lateral variations of shear wave attenuation in the upper mantle. *Journal of Geophysical Research: Solid Earth*, *101*(B10), 22273–22289. https://doi.org/10.1029/96JB01782

Burke, K. (2011). Plate Tectonics, the Wilson Cycle, and Mantle Plumes: Geodynamics from the Top. *Annual Review of Earth and Planetary Sciences*, *39*, 1–29. https://doi.org/10.1146/annurev-earth-040809-152521

Burke, K., & Torsvik, T. H. (2004). Derivation of Large Igneous Provinces of the past 200 million years from long-term heterogeneities in the deep mantle. *Earth and Planetary Science Letters*, *227*(3), 531–538. https://doi.org/10.1016/j.epsl.2004.09.015

Cottaar, S., & Lekic, V. (2016). Morphology of seismically slow lower-mantle structures. *Geophysical Journal International*, *207*(2), 1122–1136. https://doi.org/10.1093/gji/ggw324

Crotwell, H. P., Owens, T. J., & Ritsema, J. (1999). The TauP Toolkit: Flexible Seismic Travel-time and Ray-path Utilities. *Seismological Research Letters*, *70*(2), 154–160. https://doi.org/10.1785/gssrl.70.2.154

Dalton, C. A., Ekström, G., & Dziewoński, A. M. (2008). The global attenuation structure of the upper mantle. *Journal of Geophysical Research: Solid Earth*, *113*(B9). https://doi.org/10.1029/2007JB005429

Davaille, A., & Romanowicz, B. (2020). Deflating the LLSVPs: Bundles of Mantle Thermochemical Plumes Rather Than Thick Stagnant "Piles." *Tectonics*, *39*(10), e2020TC006265. https://doi.org/10.1029/2020TC006265

Dobrosavljevic, V. V., Zhang, D., Sturhahn, W., Chariton, S., Prakapenka, V. B., Zhao, J., Toellner, T. S., Pardo, O. S., & Jackson, J. M. (2023). Melting and defect transitions in FeO up to pressures of Earth's core-mantle boundary. *Nature Communications*, *14*(1), 7336. https://doi.org/10.1038/s41467-023-43154-w

Dziewoński, A. M., & Anderson, D. L. (1981). Preliminary reference Earth model. *Physics of the Earth and Planetary Interiors*, *25*(4), 297–356. https://doi.org/10.1016/0031-9201(81)90046-7

Dziewoński, A.M., Forte, A.M., Su, W., and Woodward, R.L., (1993). Seismic tomography and geodynamics. *Geophysical Monograph Series*, *76*, pp.67-105. https://agupubs.onlinelibrary.wiley.com/doi/epdf/10.1029/GM076p0067

French, S. W., & Romanowicz, B. (2015). Broad plumes rooted at the base of the Earth's mantle beneath major hotspots. *Nature*, *525*(7567), 95–99. https://doi.org/10.1038/nature14876

Garnero, E. J., McNamara, A. K., & Shim, S.-H. (2016). Continent-sized anomalous zones with low seismic velocity at the base of Earth's mantle. *Nature Geoscience*, *9*(7), 481–489. https://doi.org/10.1038/ngeo2733

Guerrero, J. M., Deschamps, F., Hsieh, W.-P., & Tackley, P. J. (2024). The combined effect of heterogeneous thermal conductivity, chemical density contrast, and heat-producing element enrichment on the stability of primordial reservoirs above the core-mantle boundary. *Earth and Planetary Science Letters*, *637*, 118699. https://doi.org/10.1016/j.epsl.2024.118699

Jackson, D. D., & Anderson, D. L. (1970). Physical mechanisms of seismic-wave attenuation. *Reviews of Geophysics*, *8*(1), 1–63. https://doi.org/10.1029/RG008i001p00001

Karaoğlu, H., & Romanowicz, B. (2018). Inferring global upper-mantle shear attenuation structure by waveform tomography using the spectral element method. *Geophysical Journal International*, *213*(3), 1536–1558. https://doi.org/10.1093/gji/ggy030

Kellog, L. H., Hager, B. H., & van der Hilst, R. D. (1999). *Compositional Stratification in the Deep Mantle | Science*, 283(5409), 1881-1884. Retrieved April 28, 2025, from https://www.science.org/doi/10.1126/science.283.5409.1881

Koelemeijer, P., Deuss, A., & Ritsema, J. (2017). Density structure of Earth's lowermost mantle from Stoneley mode splitting observations. *Nature Communications*, *8*(1), 15241. https://doi.org/10.1038/ncomms15241

Lai, H., & Garnero, E. J. (2020). Travel Time and Waveform Measurements of Global Multibounce Seismic Waves Using Virtual Station Seismogram Stacks. *Geochemistry, Geophysics, Geosystems*, *21*(1), e2019GC008679. https://doi.org/10.1029/2019GC008679

Lai, H., Garnero, E. J., Grand, S. P., Porritt, R. W., & Becker, T. W. (2019). Global Travel Time Data Set From Adaptive Empirical Wavelet Construction. *Geochemistry, Geophysics, Geosystems*, *20*(5), 2175–2198. https://doi.org/10.1029/2018GC007905

Lawrence, J. F., & Wysession, M. E. (2006). Seismic Evidence for Subduction-Transported Water in the Lower Mantle. In *Earth's Deep Water Cycle* (pp. 251–261). American Geophysical Union (AGU). https://doi.org/10.1029/168GM19

Lee, C.-T. A., Luffi, P., Höink, T., Li, J., Dasgupta, R., & Hernlund, J. (2010). Upside-down differentiation and generation of a 'primordial' lower mantle. *Nature*, *463*(7283), 930–933. https://doi.org/10.1038/nature08824

Lekić, V. (2012) *Clustering of Lower Mantle Structure – Perm Anomaly – Seismological Laboratory at the University of Maryland*. (2012). Retrieved November 7, 2024, from https://www.geol.umd.edu/facilities/seismology/data/clustering-of-lower-mantle-structure-perm-anomaly/

Lekić, V., Matas, J., Panning, M., & Romanowicz, B. (2009). Measurement and implications of frequency dependence of attenuation. *Earth and Planetary Science Letters*, *282*(1), 285–293. https://doi.org/10.1016/j.epsl.2009.03.030

Li, X.-D., & Romanowicz, B. (1996). Global mantle shear velocity model developed using nonlinear asymptotic coupling theory. *Journal of Geophysical Research: Solid Earth*, *101*(B10), 22245–22272. https://doi.org/10.1029/96JB01306

Liu, Y., Yang, T., Wang, K., Wang, X., & Li, Y. (2024). Influence of Grain Size Evolution on Mantle Plume and LLSVP Dynamics. *Geochemistry, Geophysics, Geosystems*, *25*(11), e2024GC011807. https://doi.org/10.1029/2024GC011807

Liu, Z., Fei, H., Chen, L., McCammon, C., Wang, L., Liu, R., Wang, F., Liu, B., & Katsura, T. (2021). Bridgmanite is nearly dry at the top of the lower mantle. *Earth and Planetary Science Letters*, *570*, 117088. https://doi.org/10.1016/j.epsl.2021.117088

Masters, T. G., Johnson, S., Laske, G., Bolton, H., & Davies, J. H. (1997). A shear—Velocity model of the mantle. *Philosophical Transactions of the Royal Society of London. Series A: Mathematical, Physical and Engineering Sciences*, *354*(1711), 1385–1411. https://doi.org/10.1098/rsta.1996.0054

Masters, G., Laske, G., Bolton, H. and Dziewoński, A., (2000). The relative behavior of shear velocity, bulk sound speed, and compressional velocity in the mantle: Implications for chemical and thermal structure. *Geophysical monograph series*, *117*, pp.63-87. 10.1029/GM117p0063

Matas, J., & Bukowinski, M. S. T. (2007). On the anelastic contribution to the temperature dependence of lower mantle seismic velocities. *Earth and Planetary Science Letters*, *259*(1–2), 51–65. https://doi.org/10.1016/j.epsl.2007.04.028

McNamara, A. K., & Zhong, S. (2004). Thermochemical structures within a spherical mantle: Superplumes or piles? *Journal of Geophysical Research: Solid Earth*, *109*(B7), 2003JB002847. https://doi.org/10.1029/2003JB002847

McNamara, A. K., & Zhong, S. (2005). Thermochemical structures beneath Africa and the Pacific Ocean. *Nature*, *437*(7062), 1136–1139. https://doi.org/10.1038/nature04066

Panton, J., Davies, J. H., Koelemeijer, P., Myhill, R., & Ritsema, J. (2025). Unique composition and evolutionary histories of large low velocity provinces. *Scientific Reports*, *15*(1), 4466. https://doi.org/10.1038/s41598-025-88931-3

Romanowicz, B. (1998). Attenuation Tomography of the Earth's Mantle: A Review of Current Status. *Pure and Applied Geophysics*, *153*(2), 257–272. https://doi.org/10.1007/s000240050196

Romanowicz, B. A., & Mitchell, B. J. (2015). Deep Earth Structure: *Q* of the Earth from Crust to Core. In G. Schubert (Ed.), *Treatise on Geophysics (Second Edition)* (pp. 789–827). Elsevier. https://doi.org/10.1016/B978-0-444-53802-4.00021-X

Su, W. J., Woodward, R.L., Dziewoński, A. M. (1994). Degree 12 model of shear velocity heterogeneity in the mantle *Journal of Geophysical Research: Solid Earth—Wiley Online Library*. *99*(B4), 6945-6980. Retrieved April 28, 2025, from https://agupubs.onlinelibrary.wiley.com/doi/10.1029/93JB03408

Su, W.J. and Dziewoński, A.M., 1997. Simultaneous inversion for 3-D variations in shear and bulk velocity in the mantle. *Physics of the Earth and Planetary Interiors*, *100*(1-4), pp.135-156. https://doi.org/10.1016/S0031-9201(96)03236-0

Tackley, P. J. (2012). Dynamics and evolution of the deep mantle resulting from thermal, chemical, phase and melting effects. *Earth-Science Reviews*, *110*(1), 1–25. https://doi.org/10.1016/j.earscirev.2011.10.001

Talavera-Soza, S., Cobden, L., Faul, U., & Deuss, A. (2023). Global 3D model of mantle attenuation using seismic normal modes. *Research Square.* https://doi.org/10.21203/rs.3.rs-1580818/v1

Williams, C. D., Mukhopadhyay, S., Rudolph, M. L., & Romanowicz, B. (2019). Primitive Helium Is Sourced From Seismically Slow Regions in the Lowermost Mantle *Geochemistry, Geophysics, Geosystems—Wiley Online Library*. 20(8), 4130-4145. Retrieved April 28, 2025, from https://agupubs.onlinelibrary.wiley.com/doi/10.1029/2019GC008437

Yuan, Q., Li, M., Desch, S. J., Ko, B., Deng, H., Garnero, E. J., Gabriel, T. S. J., Kegerreis, J. A., Miyazaki, Y., Eke, V., & Asimow, P. D. (2023). Moon-forming impactor as a source of Earth's basal mantle anomalies. *Nature*, *623*(7985), 95–99. https://doi.org/10.1038/s41586-023-06589-1

Zhao, C., Garnero, E. J., McNamara, A. K., Schmerr, N., & Carlson, R. W. (2015). Seismic evidence for a chemically distinct thermochemical reservoir in Earth's deep mantle beneath Hawaii. *Earth and Planetary Science Letters*, *426*, 143–153. https://doi.org/10.1016/j.epsl.2015.06.012